
Wideband RF Radiance Field Modeling Using Frequency-embedded 3D Gaussian Splatting

Zechen Li^{1*} Lanqing Yang^{1*} Yiheng Bian¹ Hao Pan^{1†}
Yongjian Fu² Yezhou Wang¹ Yi-Chao Chen¹ Guangtao Xue¹ Ju Ren³

¹Shanghai Jiao Tong University ²Central South University ³Tsinghua University

{zechlee, yanglanqing, byhbye123, panh09,
yezhouwang, yichao, gt_xue}@sjtu.edu.cn
fuyongjian@csu.edu.cn renju@tsinghua.edu.cn

Abstract

This paper presents an innovative frequency-embedded 3D Gaussian splatting (3DGS) algorithm for wideband radio-frequency (RF) radiance field modeling, offering an advancement over the existing works limited to single-frequency modeling. Grounded in fundamental physics, we uncover the complex relationship between EM wave propagation behaviors and RF frequencies. Inspired by this, we design an EM feature network with attenuation and radiance modules to learn the complex relationships between RF frequencies and the key properties of each 3D Gaussian, specifically the attenuation factor and RF signal intensity. By training the frequency-embedded 3DGS model, we can efficiently reconstruct RF radiance fields at arbitrary unknown frequencies within a given 3D environment. Finally, we propose a large-scale power angular spectrum (PAS) dataset containing 50000 samples ranging from 1 to 100 GHz in 6 indoor environments, and conduct extensive experiments to verify the effectiveness of our method. Our approach achieves an average Structural Similarity Index Measure (SSIM) up to 0.72, and a significant improvement up to 17.8% compared to the current state-of-the-art (SOTA) methods trained on individual test frequencies. Additionally, our method achieves an SSIM of 0.70 without prior training on these frequencies, which represents only a 2.8% performance drop compared to models trained with full PAS data. This demonstrates our model’s capability to estimate PAS at unknown frequencies. *For related code and datasets, please refer to <https://github.com/sim-2-real/Wideband3DGS>.*

1 Introduction

Radio frequency (RF) signals constitute various wireless systems that offer numerous conveniences in daily life. For instance, low-frequency RFID is utilized for object identification [1], 5 GHz WiFi/Bluetooth facilitates communication and device connectivity [2], and 77-81 GHz FMCW radar is employed for human motion detection [3]. Efficient comprehension of these RF signal channels is crucial for optimizing wireless systems [4]. However, due to the complex nature of RF signal propagation, modeling RF radiance fields remains a significant challenge [5–7].

Neural radiance fields (NeRF [8]), originally developed for visible light modeling using deep learning, have been extended to RF radiation field reconstruction, seen in Nerf2 [9] and NeWRF [10]. However, these approaches face issues such as high training costs, slow rendering, and limited

*Both authors contributed equally.

†Corresponding author.

interpretability [11]. Inspired by 3D Gaussian Splatting (3DGS [12–17]) technology, researchers have proposed WRF-GS [18] and RF-3DGS [19], which facilitate ease of training and fast rendering speeds while achieving reconstruction performance comparable to NeRF-based methods. However, existing works primarily focus on modeling RF radiation fields at a single frequency, despite daily scenarios often involving RF signals across wideband [20, 21]. Given that current methods use specific frequency datasets to train models, developing a wideband model based on existing work would require retraining a model for each new frequency. Additionally, these methods cannot transfer trained models to frequency bands without datasets, highlighting a key limitation. This raises a research question: Can we design a unified model to model RF radiation fields within a given 3D scene, allowing inference of radiation fields across all frequencies within a broad range?

In electromagnetic physics, reflection, transmission, and absorption are closely related to a material’s frequency-dependent permittivity and conductivity, while diffraction is highly-related to wavelength and obstacle size [22]. Consequently, EM waves of different frequencies exhibit varying propagation behaviors [23], which are strongly frequency-dependent but complex, also influenced by the environment’s 3D configuration and material properties.

This paper proposes a frequency embedding-based 3DGS algorithm for unified modeling of wideband RF radiation fields. Based on Huygens’ principle [24], we use 3D Gaussians to represent new wave sources formed when original EM waves encounter obstacles. The EM-related parameters of these Gaussian spheres, such as attenuation factor and signal intensity, are used to describe specific information about these new wave sources. We embed frequency features into the EM-related parameters of each 3D Gaussian to explore the complex relationship between these parameters and frequency. Specifically, we propose two modules, the attenuation network and the radiance network, to capture information on the attenuation and signal intensity of each 3D Gaussian under different frequencies and transmitter antenna positions. Once the entire model is adequately trained, it can interpret the RF channel information (e.g., power angular spectrum) across a wideband within a specified 3D environment. Given the position and operating frequency of a transmitting antenna, our frequency-embedded 3DGS model can determine the parameters of all Gaussian spheres, then use projection rendering and differential tile rasterization to generate the power angular spectrum (PAS) for a given receiving antenna.

We employ the NVIDIA sionna simulator [25] to generate PAS datasets in six indoor environments, covering an ultra-wideband range from 1 GHz to 100 GHz. After training on the simulated wideband dataset, our model can successfully predict the PAS of the receiving antenna at different frequency points and transmitter antenna positions within a given environment. The predicted SSIM metric shows an average improvement of 17.8% over 6 different scenes, surpassing the current SOTA method trained on individual test frequencies. This indicates that unified modeling of wideband RF radiation fields, by fully leveraging cross-band information, can enhance the model’s understanding of EM wave propagation at specific frequencies in the current 3D environment. Additionally, our model demonstrates strong capability in estimating angle power spectra at unknown frequencies, with only a 2.8% difference compared to trained frequencies. Extensive experiments verify that our model can implement unified modeling of RF radiation fields across wideband.

Our contributions are summarized as follows:

- We are the first to propose a unified RF radiance field modeling solution across wideband, introducing a frequency-embedded 3DGS model that can reconstruct power angular spectrum with any TX antenna position and frequency in a given 3D scene.
- We design the attenuation and radiance network modules with frequency embeddings to learn the frequency-dependent attenuation factor and signal intensity of each 3D Gaussian.
- We generate the novel wideband power angular spectrum dataset (1-100 GHz, 6 indoor environments, 50000 samples in total) and open-source the code and dataset.
- Extensive experiments show that our model surpasses the current SOTA by 17.8% SSIM in PAS prediction and exhibits commendable predictive capability at untrained frequencies.

2 Related Work

Modeling visible light radiance fields is a hot research area as it supports various computer vision tasks [26]. However, RF radiance fields, with frequencies much lower than visible light, are more

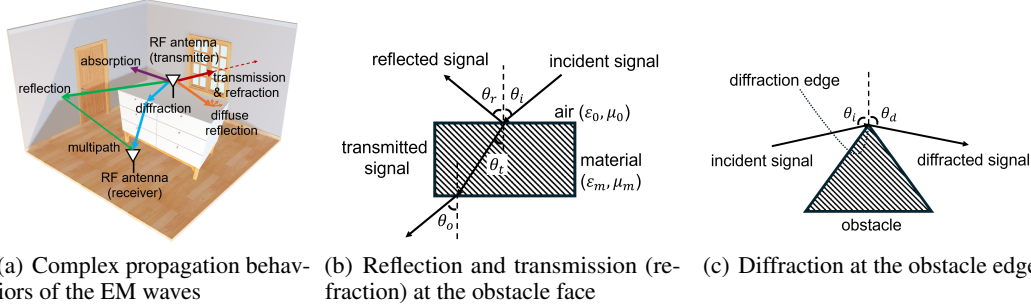


Figure 1: EM waves exhibit complex propagation behaviors that are closely influenced by factors such as materials, wavelengths, and the shapes of obstacles.

complex to model due to their intricate propagation characteristics and multipath effects [27]. Recent studies have explored deep learning for RF radiance field modeling, employing neural networks to learn the complex wireless channel in the environment. Adita et al. [28] introduced a LSTM/GRU-based autoencoders to predict the wireless channel quality. Liu et al. [29] proposed FIRE, utilizing variational autoencoders (VAE) to estimate the downlink channel information from the uplink. Inspired by the NeRF [8], several studies have applied it to RF radiance field modeling [10, 19, 30]. Orekondy et al. [30] presented a neural surrogate model based on NeRF to simulate EM propagation behaviors indoors. Zhao et al. [19] proposed NeRF2, a wireless radiance reconstruction method based on NeRF, to predict the power angular spectrum at receiver antennas with unmeasured transmitter antenna’s location using channel measurements collected from a real-world indoor environment for training. Lu et al. [10] proposed NeWRF to achieve wireless channel estimation of any unknown positions. However, NeRF-based methods often encounter challenges such as high computational complexity and slow synthesis speeds. Considering the advantages of 3DGS over NeRF, Wen et al. proposed WRF-GS [18], a method that substitutes the NeRF core in NeRF2 with 3DGS to enable fast training and rendering for the power angular spectrum reconstruction task. Zhang et al. presented RF-3DGS [19], which uses 3DGS to reconstruct dense wireless channel with limited measured receiving samples, given a specific 3D environment and a fixed transmitter antenna.

Existing research mainly focuses on single-frequency scenarios, resulting in a gap in wideband RF radiance field modeling. This paper aims to address this gap. Next, we first explore the relationship between EM wave propagation and frequency within a specific 3D environment, grounded in fundamental physics. Then, we introduce a frequency-embedded 3DGS model to facilitate unified modeling and reconstruction of wideband RF radiance fields.

3 Preliminary

3.1 Primer on Electromagnetics

RF radiation field reconstruction involves using sparse RF signal samples from a given environment to reconstruct the radiance field throughout the area. The reconstruction algorithm is required to understand various propagation behaviors such as reflection, transmission, refraction, diffraction, and absorption. Moreover, the multipath effect occurs when EM waves from the same transmitting (TX) antenna travel along multiple paths and combine at the receiving (RX) antenna; this effect can lead to signal enhancement or attenuation. The complex propagation behaviors, as shown in Fig. 1(a), make RF modeling more challenging than modeling visible light. In this section, we will methodically analyze these propagation behaviors and explore their correlation with frequencies.

As EM waves travel through the air with a distance d , their path loss is influenced by the frequency (f): $pathloss = 20 \log_{10} \frac{4\pi df}{c}$, where c is the speed of light. When encountering an obstacle, as shown in Fig. 1(b), waves may reflect, transmit, or be absorbed. This behavior is primarily determined by the material’s permittivity (ϵ_m) and conductivity (μ_m). Utilizing equivalent circuit models [31] and S-parameter formulas [32], we can derive reflection rate (R) as $R = \left| \frac{\sqrt{\eta_m} - \sqrt{\eta_0}}{\sqrt{\eta_m} + \sqrt{\eta_0}} \right|^2$, transmission rate (T) as $T = \left| \frac{2\sqrt{\eta_0}}{\sqrt{\eta_m} + \sqrt{\eta_0}} \right|^2$, and absorption (A) as: $A = 1 - R - T$. Among them, $\eta_m = \frac{\mu_m}{\epsilon_m}$, $\eta_0 = \frac{\mu_0}{\epsilon_0}$, where ϵ_0 and μ_0 are the permittivity and conductivity of the air. We can derive the relationship between the angle of refraction (i.e., transmission in the obstacle) θ_t and the angle of incidence θ_i :

$\frac{\sin(\theta_t)}{\sin(\theta_i)} = \sqrt{\frac{\epsilon_m \mu_m}{\epsilon_0 \mu_0}}$. It is important to note that these parameters, ϵ and μ , of any material depend on frequency and can be represented as $\epsilon(f)$ and $\mu(f)$ [33]. Thus, we conclude that reflection, transmission (refraction), and absorption of EM waves when encountering obstacles are related to material’s frequency-dependent properties.

When EM waves encounter the edges of an obstacle, diffraction occurs, as illustrated in Fig. 1(c). Using the Uniform Theory of Diffraction (UTD) [34], we can express the relationship between the diffracted EM field (E_d) and the incident EM field (E_i) in a simplified form: $E_d = E_i D(\theta_i, \theta_d, k, \epsilon_m, \mu_m) F$, where θ_i is the incident angle, θ_d is the diffracted angle, k is wavenumber: $k = \frac{2\pi f}{c}$. The diffraction factor $D(\cdot)$ describes changes in an EM wave’s amplitude and phase as it passes an edge, and F represents a polarization factor. Thus, we can also conclude that diffraction when EM waves encounter obstacle’s edges is also strongly correlated with EM wave frequency.

3.2 3D Gaussian Representation of EM Wave Propagation

The 3DGS technique is extensively used in optical radiation field reconstruction. According to the Huygens-Fresnel principle [35], each point on a wavefront acts as a secondary source, with propagation being the superposition of these secondary sources. When EM waves encounter obstacles, their propagation changes significantly, creating new EM radiation sources with distinct properties. Therefore, 3DGS is highly suitable for RF radiation field, involves modeling each 3D point on an object’s surface or edge as a 3D Gaussian and capturing the new source characteristics when the EM waves meet that point. The 3D Gaussian encompasses not only position, rotation, and weight related to its spatial attributes but also EM-related characteristics such as the attenuation factor and RF signal radiance intensity. Specifically, the signal intensity refers to the EM energy produced when the Gaussian sphere acts as a secondary wave source. The attenuation factor describes each Gaussian sphere’s hierarchical influence on EM waves reaching the receiving antenna, reflecting its role in the overall wave superposition. Thus, the EM propagation behaviors at each 3D point can be directly modeled using specific parameters of the 3D Gaussian.

3.3 Power Angular Spectrum

The RF radiation field describes the spatial distribution and propagation characteristics of EM waves. However, specific modeling often employs representations like wireless channels or power angular spectra (PAS) to characterize these fields. In this paper, we draw on NeRF2 [9] and WRF-GS [18] to design a PAS reconstruction task for assessing the model’s capability in RF radiation field modeling. Fig. 2 illustrates an example of a PAS, with the top part showing a 3D view centered on the receiving antenna array to depict the spatial angular distribution of EM waves; the bottom part is a 2D representation where the x and y axes represent azimuth and elevation angles, and color indicates RF signal energy. In this work, we define the azimuth angle range as $0 \sim 360^\circ$ and the elevation angle range as $0 - 90^\circ$ for hemispherical radiation of the receiving antenna’s direction. Thus, the PAS image dimensions are 90×360 , with each pixel representing energy information.

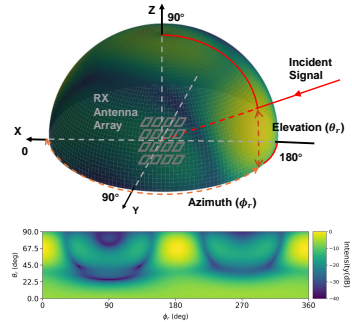


Figure 2: An example of the power angular spectrum.

4 Method Design

4.1 Overview

Modeling task: We first review the RF radiation field modeling tasks of existing works [9, 18]. Given a 3D scene with a pair of TX and RX antennas, the process of training dataset collection involves adjusting the position of the TX antenna, and recording the PAS at the RX antenna. Subsequently, the task is to utilize the measured PAS data to train a model with the capability to reconstruct the RX antenna’s PAS for any position of the TX antenna. However, these models are restricted to single-frequency point modeling.

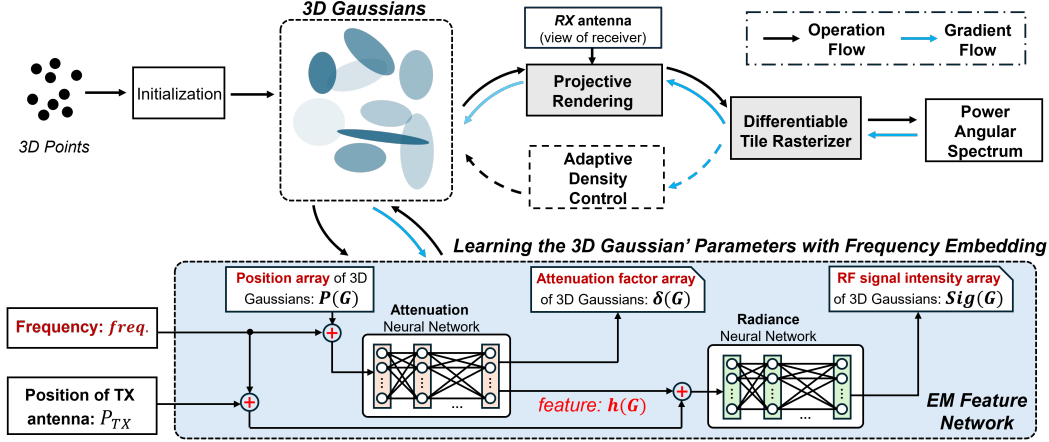


Figure 3: Architecture of the frequency embedding-based 3D Gaussian Splatting model.

To address this limitation, we propose a unified modeling task for wideband RF radiation fields. During the training data collection, when we move the TX to one position, we apply various TX antennas that operating across wideband to emit EM waves, and the corresponding various RX phased array antennas record the wideband PAS. Then, our task is to use these measured wideband PAS datasets to train a model that can reconstruct the RX antenna’s PAS for any TX antenna position and any RF frequency.

Our approach: Our model is based on 3DGS technology and incorporates frequency embedding modules to learn the complex relationship between EM wave propagation behavior and frequency. As illustrated in Fig. 3, our proposed model consists of two parts: a 3DGS model for PAS synthesis and an EM feature network for learning the feature parameters related to EM propagation within the 3D Gaussians.

We initialize the positions of the 3D Gaussians based on point cloud information from the 3D scene, while other Gaussian properties are either randomly initialized or assigned default values. The EM feature network takes as input the position of the TX antenna, the frequency value, and the positions of the 3D Gaussians, and then outputs the frequency-embedded EM propagation-related parameters, i.e., the attenuation factors and signal intensities, for all 3D Gaussians. By using a tile-based differentiable rasterizer, 3D Gaussians are splatted onto the projected RX view hemisphere to predict the PAS. During training, the loss gradient between the predicted PAS and the simulated ground truth PAS is propagated backwards to update the Gaussian properties and the parameters of the EM feature network.

4.2 Frequency-embedding Modules

In the visual rendering tasks, 3D Gaussians employ spherical harmonics (SH) to represent RGB features due to the fixed position of the light source and the varying camera poses. However, in our task, the position of the TX antenna changes during measurement, making SH function insufficient to accurately describe the complex EM wave propagation.

Considering that each 3D Gaussian represents a part of the object (e.g., mesh or edge), when an incident EM wave excite a 3D Gaussian, its characteristics, such as attenuation (δ) and signal intensity (Sig), change according to the properties of the EM waves. Firstly, the position of the TX determines the incident direction of the EM waves, which influences reflection, diffraction, and other related directions. Secondly, the frequency-dependent nature of material properties, such as relative permittivity and conductivity, affects the ratios of reflection and transmission. As a result, the attenuation and signal intensity characteristics, referred to as EM propagation features, are influenced by both the position and the operational frequency of the transmitting antenna. Conversely, the spatial features of the Gaussians, such as position, scaling, and rotation, remain invariant. This stability enables the use of machine learning methods to effectively capture the dynamically changing, frequency-dependent EM feature parameters. Thus we design an EM feature network, and it can be

expressed as follows:

$$F_{\Theta} : (P(G), P(TX), freq) \rightarrow (\delta(G), Sig(G)) \quad (1)$$

All the inputs, 3D Gaussians' positions, TX antenna's position, and the frequency, are embedded into vectors by positional encoding, then fed into the two neural networks successively. The first is an attenuation network that inputs the Gaussians $P(G)$, the TX position $P(TX)$ and the signal frequency $freq$, and outputs the hidden EM propagation feature vectors $h(G)$ and the Gaussian attenuation $\delta(G)$:

$$F_{\Theta_1} : (P(G), P(TX), freq) \rightarrow (h(G), \delta(G)) \quad (2)$$

The second module is a radiance network taking EM propagation features $h(G)$ from the attenuation network and the embedded frequency $freq$ as input to output the RF signal intensity $Sig(G)$:

$$F_{\Theta_2} : (h(G), freq) \rightarrow (Sig(G)) \quad (3)$$

The reason for using embedded frequency in both two modules is that during the learning process of Gaussian attenuation, $h(G)$ may lose some frequency information. Therefore, concatenating the embedded frequency with $h(G)$ again ensures that the radiance network can effectively utilize the frequency embedding. The detailed network structure design of these two modules is provided in the supplementary material.

4.3 RX View Projection

The PAS represents the received signal distribution of RX antenna array on a hemisphere, but the synthesis plane of 3DGS is the view projection plane of a camera. Therefore, a virtual camera imaging plane is constructed based on the RX position and orientation, then an indirect projection from the camera imaging plane onto the hemisphere of RX array is applied.

Given a point $\mathbf{P} = (x, y, z)$ in the Cartesian coordinate ($z \geq 0$), the target is to project it onto the spatial spectrum hemisphere, where the corresponding angle pixel is represented as $p = (p_x, p_y)$. The azimuth angle $\phi \in [-\pi, \pi]$ and the zenith angle $\theta \in [0, \pi/2]$ can be obtained by $\phi = atan2(x, y) = sgn(y)arctan(y/x)$ and $\theta = arccos(z/r)$, where $atan2(\cdot)$ is the four-quadrant inverse tangent function, $sgn(\cdot)$ is the sign function, and $r = \sqrt{x^2 + y^2 + z^2}$ is the Euclidean distance between P and the Cartesian origin. Then the angles can be scaled and shifted into the spectrum resolution range with $p_x = \frac{\phi + \pi}{\pi}W$ and $p_y = \frac{\theta}{\pi/2}H$, where $W \times H$ is the spectrum resolution.

4.4 Power Angular Spectrum Rendering

After 3D Gaussians are projected onto the spectrum hemisphere as 2D Gaussians, these 2D Gaussians can be used to render the PAS, similar to the differentiable tile-based rasterization algorithm of the optical 3DGS model. Since each 2D Gaussian can affect multiple pixels, splitting the PAS into tiles containing adjacent pixels instead of fine-grained pixels for parallel rendering can speed up the PAS synthesis.

Currently each Gaussian may cover multiple tiles while each tile contains multiple Gaussians. For each 2D Gaussian, if it covers t tiles, it will be instantiated for t times with a key combining its view depth and tile ID. Then these Gaussian instances are sorted by the key, creating a depth-increasing order corresponding to each tile.

For each pixel within a tile, the value of EM signal is accumulated according to the Gaussians covering it. Assuming that a pixel contains N Gaussians, the signal $Sig(G_i)$ of a Gaussian G_i should be attenuated by its former Gaussians' attenuation δ , which is between G_i and the RX. Therefore, the value of the pixel p is:

$$I(p) = \sum_{i=1}^N \left(\prod_{j=1}^{i-1} \delta(G_j) \right) Sig(G_i) \quad (4)$$

4.5 Model Training

Initiated from the scenario point clouds, the Gaussians adaptively control their density every few epochs to better reconstruct the objects in the space [36]. If a Gaussian's positional gradients are

large, it means that this Gaussian is not well-reconstructed yet. Small Gaussians indicate under-reconstruction, so they are cloned and the cloned Gaussian is moved along the direction of positional gradients, while large Gaussians imply over-reconstruction, and they are split into two smaller ones sampled from the original Gaussian. If a Gaussian’s attenuation factor δ is less than a threshold ϵ_δ , the Gaussian will be removed, as it is considered to make minimal contributions. In addition, the δ of each Gaussian is reset close to zero every few epochs as a strategy for adaptive density control and removal of useless Gaussians. The parameters of the 3D Gaussians and EM feature network are optimized by stochastic gradient descent (SGD) and the loss between predicted PAS and ground truth. The loss function is a combination of the \mathcal{L}_1 loss and the structural similarity index measure (SSIM) loss, where λ is set to 0.2:

$$\mathcal{L} = (1 - \lambda)\mathcal{L}_1 + \lambda\mathcal{L}_{SSIM} \quad (5)$$

During model training, we found that directly using the output of the attenuation module to completely replace the attenuation factor of 3DGS often leads to non-convergence and poor performance. This may be due to a conflict between the adaptive density control and the network learning process. Therefore, we retain the attenuation characteristic δ_o for each Gaussian and use the output of the attenuation network as the residual correction term δ_f . Then, $\delta_o + \delta_f$ is used as the final attenuation factor. This approach allows us to update the final attenuation factor in 3D Gaussians by learning the residual values, ensuring the model more stably and accurately reflects changes in attenuation characteristics. Thus, for the final PAS rendering and training processes, we modify Eq. 4 as follows:

$$I(p) = \sum_{i=1}^N \left(\prod_{j=1}^{i-1} (\delta_o(G_j) + \delta_f(G_j)) \right) Sig(G_i) \quad (6)$$

5 Evaluation

5.1 Dataset Description and Experiment Setup

Currently, there is no dataset available that supports the task of PAS reconstruction across wideband. To address this, we construct a large-scale simulated wideband angle power spectrum dataset that spans the frequency range of 1-100 GHz and includes 6 different indoor scenarios. Specifically, in a 3D environment, we utilize the NVIDIA sionna simulator [25] to model the propagation of EM waves emitted by the TX antenna, and employ the conventional beam forming (CBF [37]) method to generate PAS image at the location of the RX antennas. In the simulation settings, the RX is a 4×4 antenna array with each antenna being directional, while the TX antenna is a single omnidirectional antenna. In each 3D scenario, we uniformly sample 900 different TX positions and remove the inaccessible ones, allowing the RX to receive diverse signals from TX at various positions. For each TX position, we adjust the frequencies of the TX, the RX, and the materials’ permittivity and conductivity to simulate the propagation behavior of EM waves at different frequencies and generate the corresponding PAS data. In six different scenarios, we select 10 common frequency points and generate the corresponding PAS datasets. Additionally, to study the impact of a larger number of frequency points on our model’s ability of the wideband RF radiance field modeling, we select one scenario and simulate 21 frequency points that are uniformly distributed between 1 and 100 GHz. For detailed information on the data generation process and the specific parameter settings of the sionna software, please refer to the supplementary material.

For each 3D environment, we use wideband PAS images to train our proposed frequency-embedded 3DGS model and reconstruct the RF radiance field. Specifically, we divide the PAS image dataset according to the TX positions, with 80% used for training and 20% for testing. This means all frequency points in the scenario share the same training/testing TX position. Additionally, we divided the frequencies into a training set and a testing set to validate our model’s reconstruction ability at previously unseen frequencies. We use the Structural Similarity Index (SSIM [38]) between the predicted PAS image and the simulated ground truth as a criterion for quantitatively evaluating the model’s performance.

Our model is implemented in python, with both training and rendering conducted on an NVIDIA A800 GPU equipped with 80 GB of graphics memory. For access to the code, please refer to the supplementary material.

Table 1: Overall evaluation in 6 scenes at 10 frequencies

Scene	Model	Median SSIM at 10 single frequencies										Avg.
		1	2.4	5	10	24.25	37	47	60	77	94	
1	WRF-GS	0.72	0.68	0.66	0.65	0.64	0.62	0.64	0.64	0.65	0.64	0.65
	Ours	0.76	0.75	0.73	0.73	0.74	0.74	0.74	0.74	0.75	0.74	0.74
2	WRF-GS	0.54	0.54	0.50	0.55	0.54	0.52	0.51	0.52	0.51	0.51	0.52
	Ours	0.58	0.61	0.59	0.58	0.60	0.59	0.58	0.57	0.59	0.59	0.59
3	WRF-GS	0.53	0.51	0.50	0.52	0.50	0.49	0.47	0.50	0.53	0.48	0.50
	Ours	0.58	0.63	0.61	0.61	0.62	0.61	0.60	0.61	0.58	0.60	0.60
4	WRF-GS	0.60	0.58	0.54	0.52	0.54	0.55	0.54	0.53	0.51	0.54	0.55
	Ours	0.70	0.65	0.62	0.64	0.66	0.62	0.62	0.67	0.65	0.65	0.65
5	WRF-GS	0.56	0.54	0.53	0.56	0.54	0.54	0.53	0.50	0.54	0.55	0.54
	Ours	0.65	0.65	0.65	0.67	0.64	0.65	0.65	0.64	0.67	0.66	0.65
6	WRF-GS	0.64	0.61	0.60	0.61	0.58	0.61	0.57	0.61	0.60	0.59	0.60
	Ours	0.76	0.72	0.69	0.73	0.71	0.73	0.72	0.73	0.73	0.70	0.72

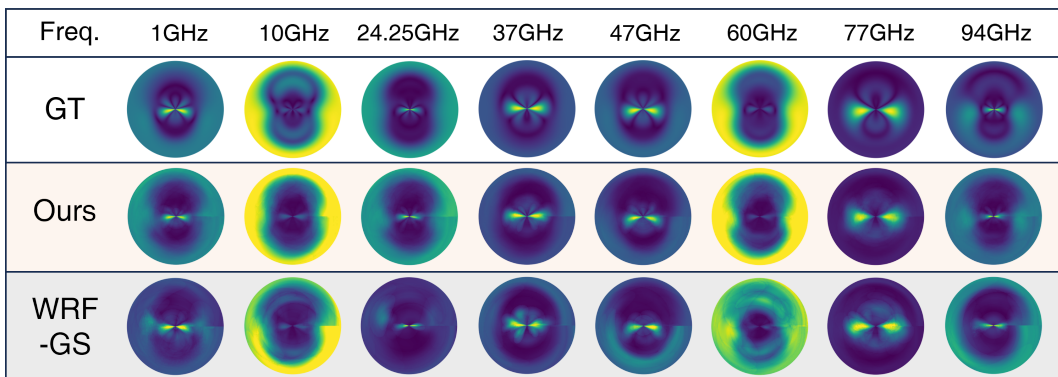


Figure 4: Overall PAS visualization at diverse frequencies and different positions.

5.2 Overall Evaluation

To validate the performance of our system, we design a series of experiments to compare it with the current SOTA method, WRF-GS [18]. Since WRF-GS can only reconstruct PAS at a single frequency, we conduct experiments on datasets across 6 scenarios and 10 frequency bands. For each 3D scenario, we train a specific WRF-GS model for each frequency and assessed its performance on the corresponding test set. In contrast, for each 3D scenario, we train our frequency-embedded 3DGS model using data from all 10 frequency bands and then evaluated its performance using test sets from each individual frequency band.

Tab. 1 presents the detailed results of the comparative experiments. Scenes 1 and 6 are indoor rooms containing simple objects, whereas scenes 2,3, 4, and 5 are more complex indoor environments with inner walls and open doors. For detailed 3D models, please refer to Fig. 5 in the appendix. As a result, the PAS prediction in scenes 2 to 5 seems to be worse than in scenes 1 and 6. However, whether in simple or complex scenarios, it is exciting to find that our proposed wideband 3DGS model outperforms the existing SOTA across every 3D scenario and frequency band. Statistical analysis shows that our method achieves an average PAS prediction SSIM of 0.66 across all frequencies, whereas the 10 specifically trained SOTA models have an average prediction SSIM of 0.56, resulting in an improvement of 17.8%. Fig. 4 presents partial visual results of PAS reconstruction. It is clear that our method not only surpasses the current SOTA in terms of the SSIM, but also visually appears closer to the GT than SOTA.

To explore model performance across more frequency points, we conduct a comparison between our model and SOTA across 21 frequencies in Scene 1. The experimental results, as shown in Fig. 7, indicate that our model achieves an average median SSIM of 0.72 across 21 frequencies, whereas the SOTA only achieves an average of 0.63. In every frequency, our model consistently outperforms the SOTA, with an average improvement of 14.3%. This confirms that our model continues to excel compared to the SOTA, even when predicting tasks involving 21 frequencies from 1 to 100 GHz.

Table 2: Cross-frequency prediction in 6 scenes at 10 frequencies, with detailed combinations C1-C4 listed in Tab. 5

Scene	C1	C2	C3	C4
1	0.75	0.74	0.73	0.70
2	0.70	0.68	0.67	0.64
3	0.67	0.66	0.63	0.58
4	0.72	0.71	0.70	0.66
5	0.70	0.69	0.63	0.63
6	0.74	0.70	0.69	0.57

Table 3: Ablation study of two modules, \checkmark/\times denotes with/without frequency-embedding

Module		SSIM	
Attenuation freq. emb.	Radiance freq. emb.	All freq.	Cross freq.
\checkmark	\checkmark	0.72	0.73
\times	\checkmark	0.71	0.71
\checkmark	\times	0.71	0.71
\times	\times	0.63	0.53

Based on the experimental results, we draw the following findings: (1) By designing a unified 3DGS model, we can effectively model the RF radiance fields across different frequency bands; (2) Our frequency-embedded 3DGS model, trained on multi-frequency PAS data, outperforms single-frequency-trained SOTA 3DGS models. This phenomenon indicates that a model capable of understanding RF radiation fields across multiple frequency bands can achieve a deeper comprehension of EM wave propagation behavior at a specific frequency in an entire 3D scene.

5.3 Cross-frequency Prediction

To explore our model’s ability to predict the PAS at unknown (i.e., untrained) frequencies, we conducted cross-frequency experiments across all 6 scenes, selecting several out of 10 frequencies as training frequencies, while the remaining frequencies were used for testing. The divisions between training and testing frequencies are detailed in Tab. 5. Note that in this experiment, we utilize all the TX positions for training in each scene. The results of the cross-frequency experiments are presented in Tab. 2. The findings indicate that (1) our model can accurately predict the PAS in a given environment at untrained frequency bands, and (2) using more training frequencies improves the performance and stability of our model.

We also conduct a cross-frequency experiment on the dataset of 21 frequencies from Scene 1. The frequency combinations are listed in Tab. 6, and results are shown in Fig. 8. We find that training with 11 selected frequencies (see Combination D in Tab. 6) can achieve results close to which uses all frequencies for training. This insight suggests that when modeling a wideband RF radiance field for a scene, selecting key frequencies for data collection can be effective. Additionally, we discover that the 1 GHz is particularly important for modeling, possibly due to its rich diffraction information.

5.4 Ablation Study

Our system incorporates frequency embeddings to learn the attenuation and signal radiance features of the 3D Gaussians. To evaluate the advantages of our proposed EM feature network with frequency embedding, we conduct another ablation studies across 21 frequencies in Scene 1, at all-frequency and cross-frequency of Combination D in Tab. 6, respectively. The results are summarized in Tab. 3, where we compare the performance of PAS reconstruction when predicting at unknown TX or unknown frequencies. It is indicated that using either the frequency-embedded attenuation network or signal radiance network can increase SSIM of 0.08 to 0.18 compared to SOTA in PAS prediction tasks. When both frequency embedding modules are used together, PAS prediction SSIM is further enhanced, with an additional improvement of 0.09 to 0.20. Each module can learn the mapping of parameters related to EM wave propagation with frequency in the 3D Gaussians, so using just one module significantly improves performance. Combining both modules for EM feature learning achieves more robust and superior performance.

6 Discussion and Conclusion

In this paper, we propose a novel frequency-embedded 3DGS model to efficiently model RF radiation fields across wideband. Our approach utilizes attenuation and radiation modules to learn frequency-dependent features within 3D Gaussians, capturing the complex relationship between the EM wave propagation and the frequency.

Acquiring wideband PAS data presents significant challenges, as it requires multiple models of transmitting antennas, as well as phased array receivers, signal sources, and spectrum analyzers that operate across different frequency bands. We utilize NVIDIA sionna simulator to generate a large-scale simulated wideband PAS dataset and conduct extensive experiments to validate our method's effectiveness. Although there is a gap between simulated and real-world data [39], the sionna, based on rigorous physical formulas, can accurately simulate the differences in EM wave propagation behavior across different frequency bands [25, 40–42]. Thus, our experimental results can affirm the feasibility of utilizing a unified model to represent wideband EM wave propagation behavior.

References

- [1] S.I. Khan, B.R. Ray, and N.C. Karmakar. Rfid localization in construction with iot and security integration. *Automation in Construction*, 159:105249, 2024.
- [2] H.W. Cho and K.G. Shin. Drew: Double-throughput emulated wifi. In *Proceedings of the 30th Annual International Conference on Mobile Computing and Networking*, pages 663–678. ACM, 2024.
- [3] F. Ding, Z. Luo, P. Zhao, et al. Milliflow: Scene flow estimation on mmwave radar point cloud for human motion sensing. In *European Conference on Computer Vision*, pages 202–221, Cham, 2024. Springer Nature Switzerland.
- [4] C. De Alwis, A. Kalla, Q.V. Pham, et al. Survey on 6g frontiers: Trends, applications, requirements, technologies and future research. *IEEE Open Journal of the Communications Society*, 2: 836–886, 2021.
- [5] Robert G Kouyoumjian and Prabhakar H Pathak. A uniform geometrical theory of diffraction for an edge in a perfectly conducting surface. *Proceedings of the IEEE*, 62(11):1448–1461, 2005.
- [6] Han Na and Thomas F Eibert. A huygens’ principle based ray tracing method for diffraction calculation. In *2022 16th European Conference on Antennas and Propagation (EuCAP)*, pages 1–4. IEEE, 2022.
- [7] James Clerk Maxwell. *A treatise on electricity and magnetism*, volume 1. Clarendon press, 1873.
- [8] Ben Mildenhall, Pratul P Srinivasan, Matthew Tancik, Jonathan T Barron, Ravi Ramamoorthi, and Ren Ng. Nerf: Representing scenes as neural radiance fields for view synthesis. *Communications of the ACM*, 65(1):99–106, 2021.
- [9] Xiaopeng Zhao, Zhenlin An, Qingrui Pan, and Lei Yang. Nerf2: Neural radio-frequency radiance fields. In *Proceedings of the 29th Annual International Conference on Mobile Computing and Networking*, pages 1–15, 2023.
- [10] Haofan Lu, Christopher Vatheuer, Baharan Mirzasoleiman, and Omid Abari. Newrf: A deep learning framework for wireless radiation field reconstruction and channel prediction. *arXiv preprint arXiv:2403.03241*, 2024.
- [11] R. Ma, S. Zheng, H. Pan, et al. Automs: Automated service for mmwave coverage optimization using low-cost metasurfaces. In *Proceedings of the 30th Annual International Conference on Mobile Computing and Networking*, pages 62–76. ACM, 2024.
- [12] Bernhard Kerbl, Georgios Kopanas, Thomas Leimkühler, and George Drettakis. 3d gaussian splatting for real-time radiance field rendering. *ACM Trans. Graph.*, 42(4):139–1, 2023.
- [13] Z. Fan, K. Wang, K. Wen, et al. LightGaussian: Unbounded 3D Gaussian Compression with 15x Reduction and 200+ FPS. *Advances in Neural Information Processing Systems*, 37: 140138–140158, 2024.
- [14] G. Fang and B. Wang. Mini-Splatting: Representing Scenes with a Constrained Number of Gaussians. In *European Conference on Computer Vision*, pages 165–181, Cham, 2024. Springer Nature Switzerland.
- [15] S. Girish, K. Gupta, and A. Shrivastava. Eagles: Efficient Accelerated 3D Gaussians with Lightweight Encodings. In *European Conference on Computer Vision*, pages 54–71, Cham, 2024. Springer Nature Switzerland.
- [16] J. C. Lee, D. Rho, X. Sun, et al. Compact 3D Gaussian Representation for Radiance Field. In *IEEE/CVF Conference on Computer Vision and Pattern Recognition (CVPR)*, pages 21719–21728. IEEE, 2024.

- [17] Michael Niemeyer, Fabian Manhardt, Marie-Julie Rakotosaona, Michael Oechsle, Daniel Duckworth, Rama Gosula, Keisuke Tateno, John Bates, Dominik Kaeser, and Federico Tombari. Radsplat: Radiance field-informed gaussian splatting for robust real-time rendering with 900+ fps. *arXiv preprint arXiv:2403.13806*, 2024.
- [18] Chaozheng Wen, Jingwen Tong, Yingdong Hu, Zehong Lin, and Jun Zhang. Wrf-gs: Wireless radiation field reconstruction with 3d gaussian splatting. *arXiv preprint arXiv:2412.04832*, 2024.
- [19] Lihao Zhang, Haijian Sun, Samuel Berweger, Camillo Gentile, and Rose Qingyang Hu. Rf-3dgs: Wireless channel modeling with radio radiance field and 3d gaussian splatting. *arXiv preprint arXiv:2411.19420*, 2024.
- [20] Xiaoyu Zhang, Weihong Pan, Chong Bao, Xiyu Zhang, Xiaojun Xiang, Hanqing Jiang, and Hujun Bao. Lookcloser: Frequency-aware radiance field for tiny-detail scene. *arXiv preprint arXiv:2503.18513*, 2025.
- [21] Douglas Paul, Michel S Nakhla, Ramachandra Achar, and Andreas Weisshaar. Broadband modeling of high-frequency microwave devices. *IEEE transactions on microwave theory and techniques*, 57(2):361–373, 2009.
- [22] John Maxwell Cowley. *Diffraction physics*. Elsevier, 1995.
- [23] Akira Ishimaru. *Electromagnetic wave propagation, radiation, and scattering: from fundamentals to applications*. John Wiley & Sons, 2017.
- [24] Bevan B Baker and Edward Thomas Copson. *The mathematical theory of Huygens' principle*, volume 329. American Mathematical Soc., 2003.
- [25] Jakob Hoydis, Sebastian Cammerer, Fayçal Ait Aoudia, Avinash Vem, Nikolaus Binder, Guillermo Marcus, and Alexander Keller. Sionna: An open-source library for next-generation physical layer research. *arXiv preprint arXiv:2203.11854*, 2022.
- [26] Kyle Gao, Yina Gao, Hongjie He, Dening Lu, Linlin Xu, and Jonathan Li. Nerf: Neural radiance field in 3d vision, a comprehensive review. *arXiv preprint arXiv:2210.00379*, 2022.
- [27] Wen Jiang, Boshu Lei, and Kostas Daniilidis. Fisherrf: Active view selection and uncertainty quantification for radiance fields using fisher information. *arXiv preprint arXiv:2311.17874*, 2023.
- [28] Adita Kulkarni, Anand Seetharam, Arti Ramesh, and J Dinal Herath. Deepchannel: Wireless channel quality prediction using deep learning. *IEEE Transactions on Vehicular Technology*, 69(1):443–456, 2019.
- [29] Zikun Liu, Gagandeep Singh, Chenren Xu, and Deepak Vasisht. Fire: enabling reciprocity for fdd mimo systems. In *Proceedings of the 27th Annual International Conference on Mobile Computing and Networking*, pages 628–641, 2021.
- [30] Tribhuvanesh Orekondy, Pratik Kumar, Shreya Kadambi, Hao Ye, Joseph Soriaga, and Arash Behboodi. Winert: Towards neural ray tracing for wireless channel modelling and differentiable simulations. In *The Eleventh International Conference on Learning Representations*, 2023.
- [31] Xiaosong Hu, Shengbo Li, and Huei Peng. A comparative study of equivalent circuit models for li-ion batteries. *Journal of Power Sources*, 198:359–367, 2012.
- [32] Fritz Caspers. Rf engineering basic concepts: S-parameters. *arXiv preprint arXiv:1201.2346*, 2012.
- [33] David J. Griffiths. *Introduction to Electrodynamics*. Pearson, 3rd edition, 1999.
- [34] Nicolas Tsingos, Thomas Funkhouser, Addy Ngan, and Ingrid Carlbom. Modeling acoustics in virtual environments using the uniform theory of diffraction. In *Proceedings of the 28th annual conference on Computer graphics and interactive techniques*, pages 545–552, 2001.

- [35] JR Mahan, NQ Vinh, VX Ho, and NB Munir. Monte carlo ray-trace diffraction based on the Huygens–Fresnel principle. *Applied Optics*, 57(18):D56–D62, 2018.
- [36] G. Wu, T. Yi, J. Fang, et al. 4d gaussian splatting for real-time dynamic scene rendering. In *Proceedings of the IEEE/CVF Conference on Computer Vision and Pattern Recognition*, pages 20310–20320. IEEE, 2024.
- [37] J. Benesty, J. Chen, and Y. Huang. Conventional Beamforming Techniques. In *Microphone Array Signal Processing*, pages 39–65. Springer, 2008.
- [38] Zhou Wang, Alan C Bovik, Hamid R Sheikh, et al. Image quality assessment: From error visibility to structural similarity. *IEEE Transactions on Image Processing*, 13(4):600–612, 2004.
- [39] Clement Ruah, Osvaldo Simeone, Jakob Hoydis, and Bashir Al-Hashimi. Calibrating wireless ray tracing for digital twinning using local phase error estimates. *IEEE Transactions on Machine Learning in Communications and Networking*, 2024.
- [40] Milica Đorđević, Nenad Jevtić, and Marija Malnar. Application of the sionna software for 5g/6g physical layer simulations. In *2024 32nd Telecommunications Forum (TELFOR)*, pages 1–4. IEEE, 2024.
- [41] Jiechen Chen, Sangwoo Park, Petar Popovski, H Vincent Poor, and Osvaldo Simeone. Neuromorphic split computing with wake-up radios: Architecture and design via digital twinning. *IEEE Transactions on Signal Processing*, 2024.
- [42] Roberto Pegurri, Francesco Linsalata, Eugenio Moro, Jakob Hoydis, and Umberto Spagnolini. Toward digital network twins: Integrating sionna rt in ns3 for 6g multi-rat networks simulations. *arXiv preprint arXiv:2501.00372*, 2024.
- [43] wikipedia. 5G - Wikipedia — en.wikipedia.org. <https://en.wikipedia.org/wiki/5G>, 2025.

A Appendices

A.1 Description of Six 3D Scenes

Fig. 5 illustrates 6 common indoor scenarios used in the experiments. Scenarios 1 and 6 are sparsely arranged to simulate simplified indoor environments, while the remaining scenarios are more densely populated with objects, serving to evaluate the model’s performance on PAS prediction tasks under complex spatial conditions.

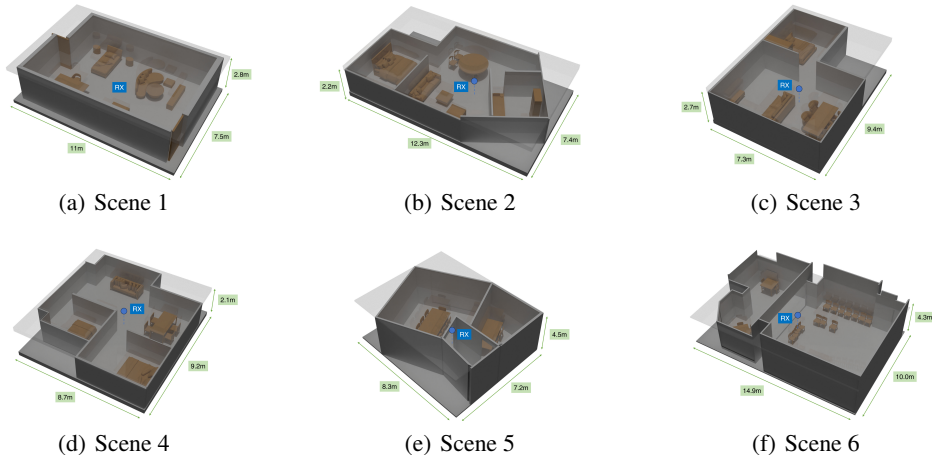


Figure 5: 6 scenes used in the experiments. The blue square indicates the position of RX.

A.2 Selected Frequencies in Wideband

We select 10 commonly used wireless signal frequencies in the daily scenarios and their representative applications. The specific frequency configurations employed in the experimental setup are determined based on this Tab. 4.

Table 4: Commonly used radio frequencies and corresponding applications [1–3, 43]

Freq. Band (GHz)	Selected Freq. (GHz)	Typical Applications
0.9 – 1.0	1.0	FM Radio, AM Radio
2.4 – 2.5	2.4	Wi-Fi (802.11b/g/n), Bluetooth, Zigbee, Microwave Ovens
5.0 – 5.9	5.0	Wi-Fi (802.11a/n/ac), 5G NR (New Radio), Short-Range Radar
8.0 – 10.0	10.0	Military Radar, Satellite Communication, Weather Radar
24.25 – 27.5	24.25	5G, Point-to-Point Communication
37.0 – 40.0	37.0	5G, Automotive Radar, Industrial Sensors
47.0 – 50.0	47.0	5G, Satellite Communication, Point-to-Point Links
57.0 – 64.0	60.0	WiGig (802.11ad), Short-Range Wireless Communication
76.0 – 81.0	77.0	Automotive Radar, 5G, Short-Range Communication
92.0 – 95.0	94.0	Radar Systems, High-Resolution Imaging, 5G

A.3 Training Loss and Model Convergence

Fig. 6 displays the training loss curves of the models trained across 6 scenes. The yellow line in the figure represents the moving average of the training loss. Since each PAS sample is treated as an individual “epoch” and the loss varies significantly across different spectrogram, the raw loss curve exhibits noticeable fluctuations. To evaluate loss stabilization, we applied a moving average with a window size of 7500 as the primary metric. As shown in the figure, the smoothed loss curves across all scenarios eventually stabilize, confirming the convergence of our training process.

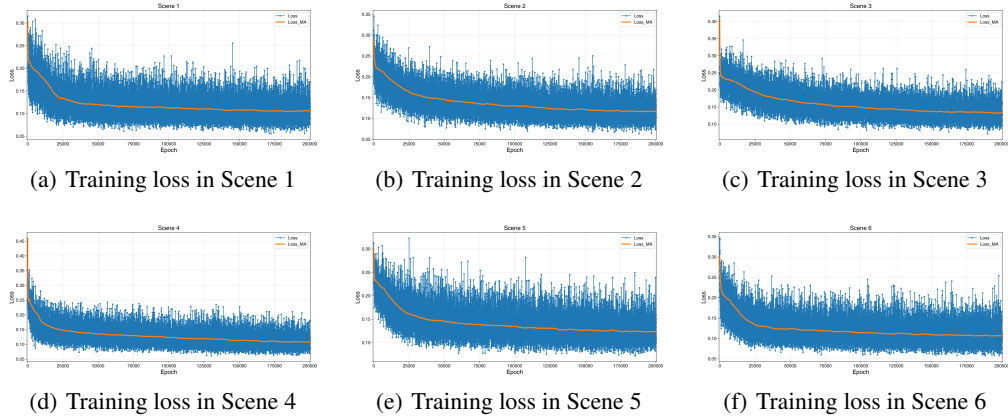


Figure 6: Visualization of training loss over epochs in 6 scenes

A.4 Overall Model Comparison with 21 Frequencies

As seen in Fig. 7, our method achieves an average median SSIM of 0.72 (± 0.007) across all 21 test frequencies (1-100 GHz) in Scene 1, outperforming the single-frequency SOTA baseline (0.63 \pm 0.016) by 14.3%. Furthermore, we observe the following: (1) our model is a robust generalization to extreme mmWave bands (0.71 SSIM at 70 GHz vs. SOTA’s 0.61), (2) our model achieves maximum gain at 25 GHz (0.73 vs. 0.65), demonstrating effective multi-frequency learning, and (3) our model achieves a lower variance (0.007 vs. 0.016) confirming our stable cross-band rendering. This validates the ability of our model to generalize across frequencies without the need for retraining.

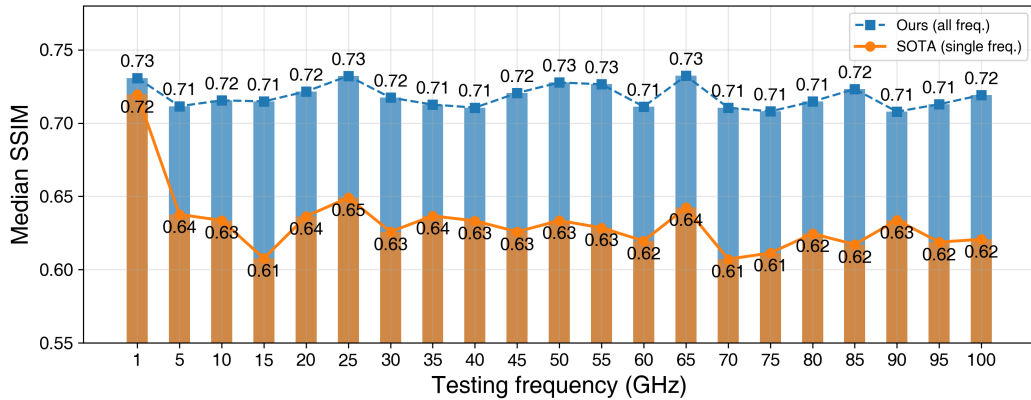


Figure 7: Overall evaluation at 21 frequencies in Scene 1.

A.5 Detailed Train/Test Frequency Combinations

Tab. 5 systematically evaluates model generalization through four training-testing frequency splits spanning 1-100 GHz. Combinations C1-C4 progressively reduce training frequencies (from 7 to 2 frequencies) while expanding testing ranges (from 3 to 8 frequencies), creating controlled scenarios to assess interpolation (e.g., C1’s 5 GHz test between 2.4-10 GHz trains) and extrapolation capabilities (e.g., C4’s 77 GHz test beyond 94 GHz trains). This hierarchy tests performance degradation under sparse supervision, covering both common wireless standards (2.4/5/24.25 GHz) and mmWave extremes (37/47/60/77/94 GHz).

Table 5: Combinations of 10 frequencies

Combination	Training frequencies (GHz)	Testing frequencies (GHz)
C1	1, 2.4, 10, 24.25, 47, 60, 94	5, 37, 77
C2	1, 5, 24.25, 47, 77	2.4, 10, 37, 60, 94
C3	1, 24.25, 77	2.4, 5, 10, 37, 47, 60, 94
C4	1, 94	2.4, 5, 10, 24.25, 37, 47, 60, 77

Tab. 6 presents the specific frequency combinations used for different experimental setups, along with the frequencies on which the testing was conducted. Combinations A, B, and C utilize data from 20 frequencies and are tested on a specific frequency to simulate the zero-shot capability of a model that has already been extensively trained on multiple frequencies for predictions on a novel frequency. Combinations D, E, F, G, and H involve progressively fewer frequencies to evaluate the impact of varying frequency combinations on the model’s generalization across frequencies. Combinations I, J, and K are trained exclusively on single-frequency data, and their predictions are tested across all remaining 20 frequencies, serving as a baseline for assessing the model’s generalization performance on unseen frequencies.

Table 6: Combinations of 21 frequencies in Scene 1

Combination	Training frequencies (GHz)	Testing frequencies (GHz)
A	5, 10, 15, 20, 25, 30, 35, 40, 45, 50, 55, 60, 65, 70, 75, 80, 85, 90, 95, 100	1
B	1, 5, 10, 15, 20, 25, 30, 35, 40, 45, 55, 60, 65, 70, 75, 80, 85, 90, 95, 100	50
C	1, 5, 10, 15, 20, 25, 30, 35, 40, 45, 50, 55, 60, 65, 70, 75, 80, 85, 90, 95	100
D	1, 10, 20, 30, 40, 50, 60, 70, 80, 90, 100	5, 15, 25, 35, 45, 55, 65, 75, 85, 95
E	1, 25, 50, 75, 100	5, 10, 15, 20, 30, 35, 40, 45, 55, 60, 65, 70, 80, 85, 90, 95
F	1, 50, 100	5, 10, 15, 20, 25, 30, 35, 40, 45, 55, 60, 65, 70, 75, 80, 85, 90, 95
G	1, 100	5, 10, 15, 20, 25, 30, 35, 40, 45, 50, 55, 60, 65, 70, 75, 80, 85, 90, 95
H	25, 75	1, 5, 10, 15, 20, 30, 35, 40, 45, 50, 55, 60, 65, 70, 80, 85, 90, 95, 100
I	100	1, 5, 10, 15, 20, 25, 30, 35, 40, 45, 50, 55, 60, 65, 70, 75, 80, 85, 90, 95
J	50	1, 5, 10, 15, 20, 25, 30, 35, 40, 45, 55, 60, 65, 70, 75, 80, 85, 90, 95, 100
K	1	5, 10, 15, 20, 25, 30, 35, 40, 45, 50, 55, 60, 65, 70, 75, 80, 85, 90, 95, 100

A.6 Cross-frequency Experimental Results Involving 21 Frequencies

Fig. 8 and Tab. 6 jointly characterize the model performance on combinations (A–K) of 21 frequencies in Scene 1.

Frequency combinations I, J, and K demonstrate the prediction results of models trained on a single frequency across all other frequencies, serving as the baseline for evaluating the model’s frequency generalization capability. It is observed that the model trained at 1 GHz performs worst in predictions across the remaining 20 frequencies. Analysis reveals this is due to the inverse relationship between wavelength and frequency: the significant wavelength discrepancy of 1 GHz wireless signals compared to other frequencies leads to distinct propagation characteristics.

Frequency combinations A, B, and C show predictions on a specific frequency using models trained on 20 frequencies, testing zero-shot capability for novel frequencies. The worst performance occurs

at 1 GHz (consistent with the above explanation), while predictions at 50 GHz and 100 GHz achieve average SSIM scores of 0.71. This represents only a marginal decline compared to the full-frequency model’s performance (0.73 and 0.72, respectively), demonstrating strong zero-shot capability for frequencies with propagation characteristics similar to the training set.

Frequency combinations D-H evaluate generalization when trained on partial frequency subsets. When half of the 21 frequencies are used (combination D), the average SSIM for unseen frequencies is 0.70, a 2.8% decrease compared to the full-frequency model’s 0.72. As fewer frequencies are included (combinations E-H), generalization gradually declines. However, all partial combinations significantly outperform the single-frequency baseline (combination H: 0.62 with two frequencies vs. combination I: average SSIM 0.56), proving that multi-frequency training enhances cross-frequency generalization.

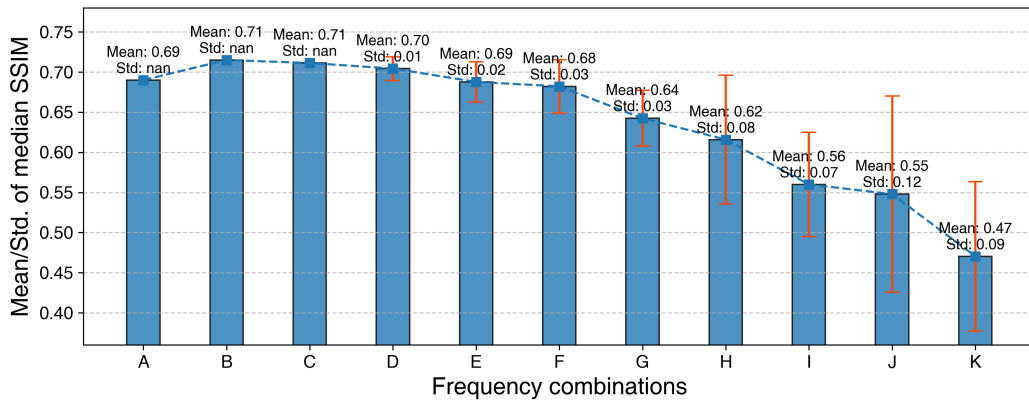


Figure 8: Cross-frequency prediction of different combinations of 21 frequencies in Scene 1. Std: nan indicates using only one testing frequency.